Depth of Penetration of Hypervelocity Projectiles

T. D. RINEY*
General Electric Company, King of Prussia, Pa.

The equations governing the visco-plastic model of hypervelocity impact and a numerical procedure for their solution are described. Preliminary calculations show that strength and strain-rate effects are unimportant during the early stages of the cratering process although they predominate during the late stages. Calculations are presented describing the flow field for a cylindrical projectile impacting a thick target of like metal. It is shown that momentum scaling cannot be justified; energy scaling for geometrically similar impact situations is predicted. The depth of penetration is therefore related to impact velocity v_0 according to $P_c = K_e v_0^{2/3}$ for v_0 greater than a threshold value for energy scaling. Strength effects of the target do not vanish with increasing impact velocity.

Nomenclature

τ_{ij}	=	stress tensor
δ_{ij}	=	unity when $i = j$, zero otherwise
D_{ij}	=	strain-rate tensor
D^2	=	second invariant of strain-rate deviator tensor
τ^2	=	second invariant of stress deviator tensor
μ	=	strain-rate coefficient
S_0	=	yield value of shear stress
η_0	=	viscosity factor in strain-rate coefficient
ρ	=	density of medium
ρ_0	=	density of undisturbed medium
I	=	specific internal energy of medium
(r, θ, z)	=	cylindrical coordinates
$(u, 0, v)$	=	velocity components in cylindrical coordinates
τ_{zz}	=	longitudinal stress in one-dimensional case
X	=	compression ratio across a shock ($= \rho_0/\rho$)
v_0	=	impact velocity
v_0'	=	impact velocity with geometry scaled to compare with v_0
v_0^*	=	threshold value for energy scaling
L	=	radius of cylindrical projectile
l	=	length of cylindrical projectile
h	=	thickness of plate target
Z_+	=	total forward axial momentum
R_+	=	total outward radial momentum
Δt	=	time lag between cratering processes
t_1	=	time for edge rarefaction to catch shock front in target at the axis
t_2	=	time for edge rarefaction to catch shock front in projectile at the axis
R_1	=	position of shock front in target at t_1
R_2	=	position of shock front in projectile at t_2
t_i	=	time for edge rarefaction to first reach axis at moving interface
R_i	=	position of interface at t_i
τ_1	=	time required for shock in projectile to reach its rear surface
l_0	=	projectile length for which $t_2 = \tau_1$
h_0	=	target depth at which edge rarefaction reaches axis in target simultaneously with the shock
D_s	=	diameter of sphere having volume equal to that of the projectile
P_c	=	penetration depth of crater

Introduction

FOR satellites and for manned space flight, the presence of meteoritic material in space accounts for one of the important environmental hazards. The velocity of the meteoroids is estimated to range from 0.5 to 7.2 cm/μsec.† A similar problem, potentially, is the damage that may be inflicted on a ballistic missile by high-speed particles produced and directed by artificial means. For these reasons, increasing attention has been focussed in recent years on the problems attendant to the collision of a projectile and a target in the hypervelocity regime.

Laboratory techniques at present are only capable of producing reliable data at velocities of less than about 1.0 cm/μsec. A great deal of data are available describing the craters formed in semi-infinite targets at these lower speeds.

Several authors have fitted formulas to the composite firing results of various experimenters. Bruce[1] concluded that above a certain threshold velocity v_0^* the depth of penetration of a projectile in a semi-infinite target varies with the impact velocity according to $P_c = C_1 v_0^{2/3}$. Herrman and Jones[2] found that an empirical fit from very low velocity data to the highest velocity data available could be obtained using a two parameter expression of the form $P = C_2 \ln(1 + C_3 v_0^2)$. They also found that the upper end of the experimental data could be fitted by a power law with exponent $n = \frac{2}{3}$. Others have obtained power law fits where the experimental data were divided into low and high velocity ranges, divided at the bulk sonic wave velocity of the target.[3] They used exponents of $n = 1$ and $n = \frac{2}{3}$ to fit the low velocity data and high velocity data, respectively.

These empirical fits are useful for *interpolation* purposes within the velocity ranges covered by the data. Without a rational theoretical basis, however, the empirical fits furnish no more information than is contained in the experimental data. *Extrapolation* to other materials or to velocities greater than about 1.0 cm/μsec is hazardous if based solely on such formulas.

The first serious attempt to calculate the phenomenology of hypervelocity impact from basic physical assumptions was made by Bjork.[4] Bjork used a hydrodynamical model and treated the rotationally symmetric case of two-dimensional, unsteady, compressible flow in a semi-infinite target under normal impact by a cylindrical projectile of the same material. Such calculations provide the shock-wave time history and the flow of material behind it. For the surface representing the final crater radius, Bjork chose the instant when a stationary region of relatively low pressure was approximated and identified this region by the appearance of a distribution of small velocities that are randomly orientated. On this basis he concluded that the penetration depth for velocities of 0.5 to 7.2 cm/μsec varies according to the power law but with $n = \frac{1}{3}$.

Received April 21, 1964; revision received August 31, 1964. This work was supported by the Air Proving Ground Center, Eglin Air Force Base, under Contract No. AF 08(635)-3781.

* Mathematician-Space Mechanics, Missile and Space Division, Space Sciences Laboratory. Member AIAA.

† The gram-centimeter-microsecond system of units is used throughout this paper. The unit of stress becomes the megabar (Mbar).

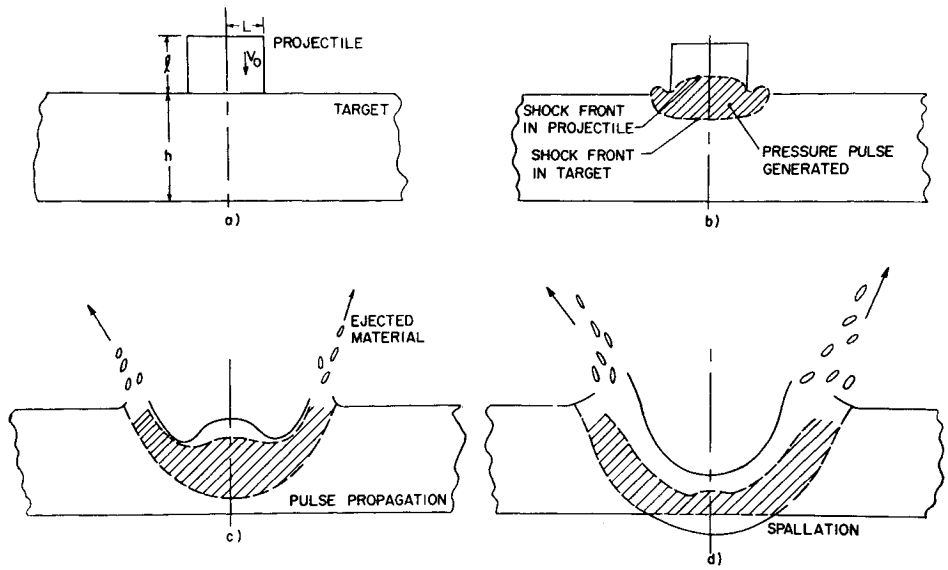

Fig. 1 Illustration of the cratering and penetration of a structural member by a hypervelocity projectile: a) axial section of configuration at impact, b) generation of pressure pulse between shock fronts in projectile and target, c) material ejected from target surface and the pressure pulse propagates into the target, and d) spallation at opposite free surface resulting from reflection of pressure pulse.

For several years researchers in the hypervelocity field remained divided in their conclusions. Some investigators adhered to the $\frac{2}{3}$ power extrapolation of empirical fits to the data, and others relied on the predictions of Bjork.

During the past year Walsh and Tillotson[5] employed the inviscid fluid model and also used the same basis numerical scheme used by Bjork. They recognized, however, that the hydrodynamic approximation alone becomes invalid in the latter stages of the crater formation because the influence of the target's strength can no longer be neglected. They terminated the hydrodynamic calculations at a pressure of 1 Mbar and then demonstrated how the results can be used, together with experimental data and an equivalence principle, to establish an expression for crater depth.

The equivalence principle used by Walsh and Tillotson states that, if, at any time during the formation of craters resulting from two different impacts, the flow fields are identical, then the subsequent reaction of the target to the action of the pressure pulses will also be identical. By application of this principle they reject the $n = \frac{1}{3}$ conclusion of Bjork and arrive at the value $n = 0.62$ that more nearly corresponds to the empirical formulas espoused by many experimentalists.

If two flow fields in a given material are truly identical at any stage, then their subsequent effects on the target must certainly be identical. Questions only arise as to the accuracy of their calculations and the degree that the calculations are identical. The impasse of the theorists at the recent Sixth Hypervelocity Symposium has been described in detail by Eichelberger[6] and discussed by Heldenfels and Hurlich[7] in their recent review article.

In this paper calculations are presented describing the cratering process for a cylindrical projectile impacting a thick target of like metal (Fig. 1). It is shown that momentum scaling cannot be justified and that energy scaling for geometrically similar impact situations is accurately predicted upon taking into account the different rates of shock propagation during the early stages of the cratering process.

Visco-Plastic Model

Since the establishment of a crater of fixed size implies that material has been brought to rest, it seems clear that at large time a transition must actually be made from the hydrodynamical model to a theory that accounts for the strength of the target. For, the inviscid hydrodynamic model itself predicts pressures comparable to or less than the shear strength of the target during the later stages of flow. A visco-plastic model has evolved which bridges the transition from the early stages, when the hydrodynamic model is a good approximation of the phenomenon, to the later stages when strain-rate and strength effects must be included in the description.[8, 9] The model neglects elastic and strain-hardening effects and assumes that the stress tensor τ_{ij} and the strain-rate tensor D_{ij} are related by a constitutive relation of the form

$$\tau_{ij} = -p\delta_{ij} + \mu(D_{ij} - \tfrac{2}{3}\,\mathrm{div}\mathbf{u}\,\delta_{ij}) \qquad (1)$$

where p is the thermodynamic pressure, μ the flow resistance coefficient, and $\mathbf{u}$ is the velocity vector. Given the required relations for p and μ, (1) may be incorporated into the partial differential equations expressing conservation of mass, momentum, and energy to obtain the system of equations governing the model (see Appendix).

Realistic expressions for the thermodynamic pressure as a function of the density ρ and specific internal energy I,

$$p = g(\rho,I) \qquad (2)$$

have been constructed from theoretical considerations and from experimental studies of one-dimensional stress pulses induced by metal-metal impact of two plates, the one propelled by a high explosive.‡ All common metals have been fitted by the same form of the expression $g(\rho,I)$, only the values of the constants occurring vary from metal to metal.

The principal uncertainty in the visco-plastic model is the lack of data on strain-rate effects under the extreme conditions operative during hypervelocity impact. The bulk of the studies with attention to strain-rate effects are for the cases in which longitudinal plastic stress waves of relatively low amplitude are propagated along bars. The maximum strain-rates obtained are of order 10^{-3} to 10^{-2} $1/\mu$sec, and the resulting data have been fitted into a polytropic framework. Several empirical relations between stress and strain-rate have been proposed which have proved adequate under conditions similar to those in which the data were generated. These rate-dependent, rigid-plastic relations may, in the absence of more realistic information, reasonably be applied in the later stages of flow in the applications of interest here.

Some of the available experimental data have been brought together within a framework general enough to permit the extrapolation of these one-dimensional empirical formulas in a

‡ The equation-of-state fit was made by R. K. Osborne and his associates in group W-4 at Los Alamos. The expression $g(\rho,I)$ and the constants for several metals are given in Refs. 9 and 10.

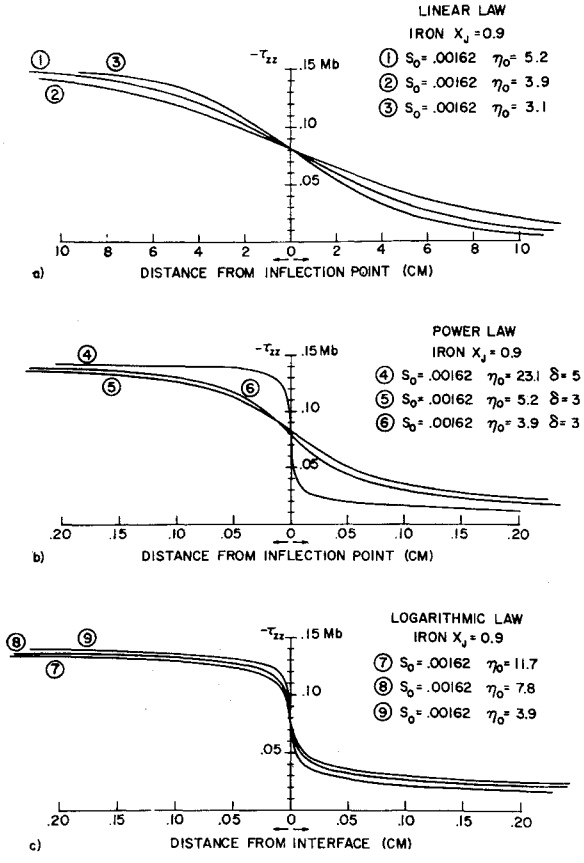

Fig. 2 Calculated shock profiles in mild steel for a final compression ratio $X_f = 0.9$ when μ is assumed to follow a) linear law, b) power law, and c) logarithmic law.

natural manner to the tri-axial case. Three of the expressions considered are as follows§:

Linear Law

$$\mu = (S_0/|D|)\ [1 + (\eta_0/S_0)|D|] \tag{3a}$$

Power Law

$$\mu = (S_0/|D|)1 + \{[\eta_0/S_0)|D|]\}^{1/\delta} \tag{3b}$$

Logarithmic Law

$$\mu = (S_0/|D|)\ 1 + \ln\{[1 + (\eta_0/S_0)|D|]\} \tag{3c}$$

provided $|\tau| \geqq S_0$. $\mu = \infty$ in each case when $|\tau| < S_0$. Here, D^2 and τ^2 are the second invariants of the strain-rate deviator tensor and the stress deviator tensor, respectively. In (A5) of the Appendix the expressions for D^2 and τ^2 in terms of the velocity components are defined for the axially symmetric case. The definitions are the conventional ones for fluid dynamics but twice those for plasticity theory. S_0, η_0, and δ are material constants estimated from the low amplitude plastic wave experiments.

The shape of the profile in the shock transition region for steady one-dimensional stress pulses have been calculated for a number of these extrapolated estimates for μ.[10] In Fig. 2, the calculated stress profiles are depicted for mild steel in the case that the final compression ratio is $X_f = 0.9$. The results are shown for three choices of the parameters for each of the three forms of μ. It is clear from Fig. 2a that the linear law spreads the shock too far to be realistic in the megabar range. The same is true for the power law if $\delta = 3$. The profile determined by the power law depends mainly on the choice of δ, being relatively insensitive to changes in η_0. Although the logarithmic law provides a steep front near the inflection point, it is extremely slow in reaching the asymptotic value of 0.15 Mbar.

Calculations were also made for some parameter choices in the case $X_f = 0.8$. Then the longitudinal stress at the crest of the stress pulse is $(-\tau_{zz})_f = 0.51$ Mbar, and a steady plane wave should have an extremely sharp front. The logarithmic law and the power law with $\delta = 5$ are compatible with this requirement.

On the basis of these calculations it was concluded that, of the three choices for μ, the power law with $\delta \geqq 5$ provides a reasonable choice for the flow resistance coefficient in the absence of more accurate information. The choices that are being used are:

Aluminum

$$S_0 = 0.00162 \qquad \eta_0 = 0.003 \qquad \delta = 8 \tag{4a}$$

Steel

$$S_0 = 0.00125 \qquad \eta_0 = 2.7 \qquad \delta = 6 \tag{4b}$$

These values lie within the range of values listed in Table 1 and are therefore compatible with observed strain-rate effects in plastic waves as well as the very abrupt shock profiles known to exist at higher pressures.

Method of Solution

The particle-in-cell numerical scheme developed at Los Alamos[12] for two-dimensional hydrodynamics has been extended to treat the visco-plastic equations governing the axisymmetric impact problem. A step-by-step prescription for carrying out the numerical calculations for the visco-plastic equations has been presented previously[13,14]; here the scheme will only be described in general terms.

An axial section of the projectile-target configuration is superposed by the fixed space mesh used to describe the subsequent motion of the configuration. On this plane of symmetry the cells of the space mesh appear as rectangles although each cell is actually a toroid of revolution. The projectile-target material is represented on this axial plane by discrete mass point called "particles"; each particle is actually a circle about the axis of symmetry. Each particle is assigned a fixed mass whose value is proportional to the radius of the cell within which it lies originally, i.e., at $t = 0$. The r and z coordinates of each particle are stored in the computing-machine memory. These are changed in time in accordance with the subsequent motion of the material through the fixed mesh of computational cells. The conservation of mass is therefore automatic.

At the end of nth time cycle, the mass (equal to the sum of the masses of the particles located in that cell), velocity, pressure, and specific internal energy are associated with each cell. To obtain the corresponding data at the end of the $(n + 1)$th time cycle, one makes a three-phase calculation. In phase I, the cellwise field functions are changed, neglecting the motion of the medium. Thus, the transport terms are dropped from the momentum and energy equations and (A2), (A3), and (A4) are replaced by difference formulas for computing tentative new cellwise velocity components and specific internal energy. In phase II, the mass particles are

Table 1 Ranges of values estimated by Symonds and Ting[11] for the parameters in the power law for mild steel and structural aluminum[a]

Metal	$S_0 \times 10^3$	η_0	δ
Mild steel	1.25	2.7 – 18	4–6
A1 6061-T6	1.62	0.003–0.154	4–8

[a] The estimates are based on the results of a number of experimenters and are expressed in the gram-centimeter-microsecond systems of units.

§ The original investigations on which these strain-rate laws are based are cited in Ref. 9.

moved according to the velocity of the cell in which it is located and the velocities of the neighboring cells. In moving, the particles carry their share of the cellwise energy and momentum with them; the field functions are then recalculated to account for the motion. In phase III, various functionals are computed which furnish checks on the accuracy of the calculations. For example, books are kept on the total axial momentum and total energy of the system. These quantities are rigorously conserved during the calculations of both phases I and II (no truncation error).

At the end of phase II of each time cycle, a tentative value for the pressure $\tilde{p}_{i,j}$ to be used in the next time cycle is first computed for each cell (i, j). Then the hypothesized fraction criterion is applied to the cell and, if satisfied, one sets $p_{i,j} = 0$. If the criterion is not satisfied, the metal remains a continuous medium in cell (i, j) and one sets $p_{i,j} = \tilde{p}_{i,j}$.

As time goes on, the size of the crater increases, and the stress wave propagates further into the target. More target material must then be covered by the calculation mesh than is necessary at earlier times. As the dimensions of the disturbance increase, however, sufficient resolution may be obtained by using a larger net size, in both time and space, than was permissible during the initial stages of the process. It is therefore advantageous to repartition the system during the course of a computational run. The method used is to double the linear dimensions of the cells, i.e., four of the original cells are combined to form a single enlarged cell in the new mesh. The area covered by the mesh is thus increased fourfold without increasing the number of cells in the mesh.

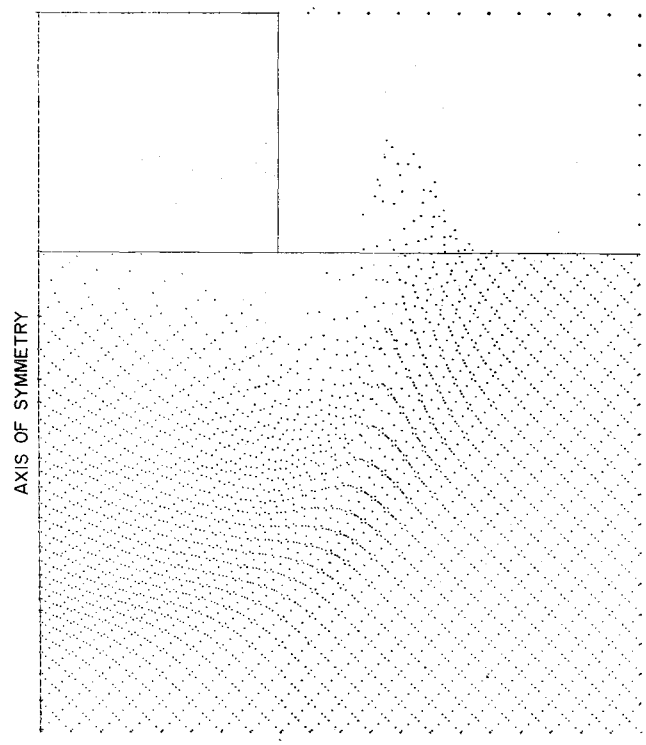

Fig. 3 The mass point plot at $t = 0.249$ μsec after impact of a cylindrical iron projectile into an iron target at $v_0 = 2.0$ cm/μsec.

Calculations with Complete Model

The computer program (PICWICK) developed to carry out the calculations is capable of using various choices for the equation of state and the flow-resistance coefficients μ. The choices (4) have been incorporated into the program and some calculations made to investigate a) the strain-rate effect in the cavitation region behind the shock front where both the pressure and strain rate are less than in the front itself, and b) the strain-rate effect on the pulse itself after it has decreased to the order of tenths of megabars and below. At the time this paper is being assembled, the calculations with the complete visco-plastic model are not complete but some conclusions may be drawn.

Calculations for both aluminum-aluminum and iron-iron impact at $v_0 = 0.76$ cm/μsec, for the choice of μ listed in (4a) and (4b), respectively, have been carried to the stage that the peak pressure has dropped below 0.3 Mbar. Only slight changes using either (4a) or (4b) are discernible when compared with the corresponding calculations with $\mu = 0$ (i.e., hydrodynamic calculations).

The fact that the inclusion of μ does not alter the flow process significantly until the pressures are well below 1 Mbar justifies continuing the hydrodynamic calculations to relatively low pressures. The limit of the validity of the hydrodynamic model probably lies between 0.04 and 0.3 Mbar since Jones, Neilson, and Benedick[15] have observed stress profiles in explosively generated plane waves in aluminum and iron up to 0.04 Mbar. They have not, however, determined the effect of varying the load level.

For pressures below about 0.2 Mbar the calculations become less accurate. The program is currently being revised to improve the resolution by the use of external storage and the replacement of the discrete mass particles by a continuous mass representation.

However, simultaneous with the investigations of the strain-rate effects, the PICWICK code has also been used extensively for the special case $\mu = 0$ in order to resolve the controversy discussed in the earlier part of this paper. These results are of immediate interest.

Calculated Flow Fields

Immediately upon impact of a metal projectile and metal target at a hypervelocity, pressures of the order of megabars are produced near the contact interface. Shock fronts originating at the contact surface then propagate upward into the projectile and downward into the target (Fig. 1). From the initial instant a rarefaction wave, originating at the periphery of the contact surface, propagates into the high-pressure region at a velocity greater than the shock velocity. The rarefaction wave thus catches up with and degrades the

Table 2 Points in time and space at which the shock fronts, rarefaction waves, and the configuration surfaces interact[a]

Point of interaction	$v_0 = 0.76$ cm/μ sec			$v_0 = 2.0$ cm/μ sec		
	Al	Fe	Pb	Al	Fe	Pb
$t_1/L = t_2/L$	1.116	0.963	1.208	0.658	0.499	0.737
R_1/L	1.178	0.963	0.938	1.188	0.945	1.142
R_2/L	0.330	0.231	0.019	−0.127	−0.053	−0.332
t_i/L	0.891	0.827	1.090	0.581	0.456	0.683
R_i/L	0.339	0.314	0.414	0.581	0.456	0.683
τ_1/l	0.947	1.000	1.289	0.553	0.528	0.645
$l_0/L = h_0/L$	1.178	0.963	0.938	1.188	0.945	1.142

[a] The vaules in this table were supplied by J. F. Heyda and are valid for like metal impact.

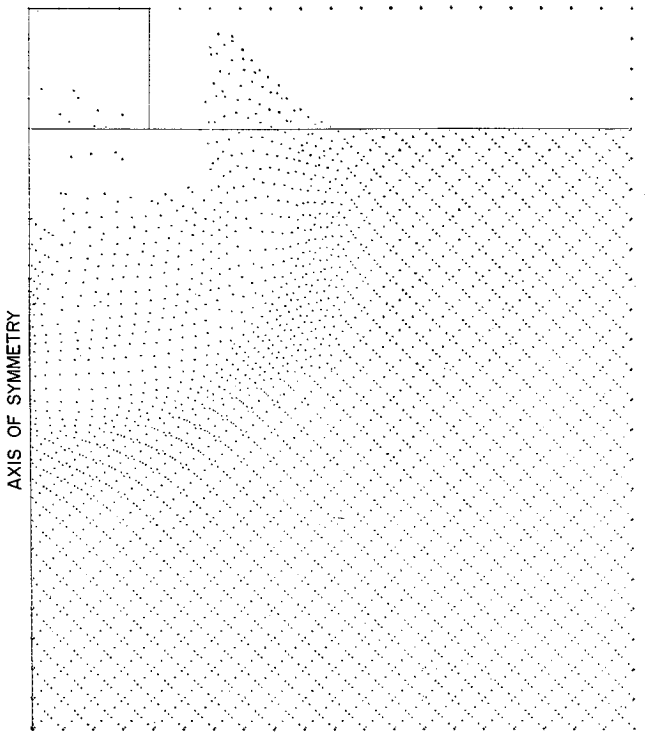

Fig. 4 The mass point plot at $t = 0.564$ μsec after impact of a cylindrical iron projectile into a thick iron target at $v_0 = 2.0$ cm/μsec.

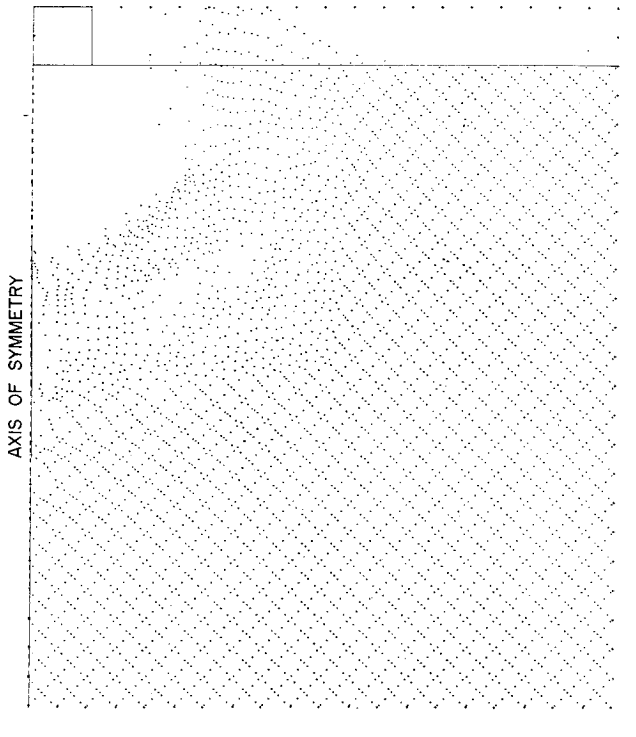

Fig. 5 The mass point plot at $t = 2.618$ μsec after impact of a cylindrical iron projectile into a thick iron target at $v_0 = 2.0$ cm/μsec.

shock fronts in the projectile and target. The edge rarefaction wave separates the unrelaxed pressure pulse into two regions upon propagating inward to the axis of symmetry. Rarefaction waves also occur when the shock fronts in projectile and target reflect at free surfaces of the projectile target configuration.

The shock dynamics during the early stages after impact of a right circular cylinder have been studied in detail.[16] It suffices here to use the results of the study in interpreting the flow fields computed using the PICWICK code. Typical calculated points in space and time at which the pressure pulse, the rarefaction waves, and the geometry interact are listed in Table 2. The definitions of the notations used there and in the following discussion are given in the Nomenclature.

Calculations have been made for like metal impact of aluminum, iron, and lead for impact velocities of $v_0 = 0.76$ and $v_0 = 2.0$ cm/μsec. In the case of aluminum, the impact velocities $v_0 = 4.0$ and 6.0 cm/μsec have also been studied. All these calculations were carried out for a cylindrical projectile of radius equal to length and a thick target ($L = l = 0.26192$ cm and $h = \infty$ in Fig. 1). The volume of the projectile is the same as that of $\frac{3}{16}$-in.-diam sphere.

The PICWICK code provides for automatic plots of the current positions of the mass particles, representing the projectile-target configuration, at any desired time cycle. In Figs. 3–5 the mass particle plots at three stages of the cratering process are depicted for iron-iron impact at $v_0 = 2.0$ cm/μsec. An outline of the original projectile-target configuration is superimposed on the plots for reference purposes. The characteristic mechanisms familiar from experimental studies are clearly illustrated by these plots. These include the formation of the backsplash at the periphery of the forming cavity and the propagation of a nearly hemispherical shock wave into the target. Some of the basic but more subtle effects that have not been observed experimentally may also be detected.

The edge rarefaction wave reaches the axis of the projectile-target configuration at time $t_1 = 0.499\ L = 0.131$ μsec. Consequently, at the time depicted in Fig. 3, $t = 0.249$ μsec, the pressure is already everywhere diminished below its one-dimensional impact value, and the shock front in the target is no longer planar even in the vicinity of the axis. The shock in the projectile has already reflected from the rear surface of the projectile at $\tau_1 \doteq 0.138$ μsec at which time the rear surface was located a distance $R_2 \doteq -0.053\text{L} = -0.039$ cm above the target surface.

Figure 4 illustrates the same calculation only at 0.564 μsec after impact. The mesh used in the computational scheme has been repartitioned to permit a greater volume of the target to be examined by the same number of computational cells. At this stage the shock in the target propagates on a nearly hemispherical front. Experimental observation of the hemispherical front is sometimes cited as justification for use of the spherically symmetric blast wave theory to describe the shock propagation. Actually the amplitude of the pressure pulse is not spherically symmetric; it decreases from a maximum value near the axis to zero at the surface of the target where it is reflected, causing material to be spalled and ejected backward from the target face.

Figure 4 also illustrates a phenomenon that always occurs in these thick target calculations. A high-density region is formed in the target about one projectile radius beneath the center of impact. From Table 2 it may be seen that for all cases considered $R_1/L \doteq 1$, and the high density region is located at the center of convergence of the edge rarefaction wave.

Figure 5 depicts the mass particle distribution at 2.618 μsec after impact. A second repartition of the computational mesh has been necessary at this stage. The nearly spherical form of the forming crater is clearly delineated.

Energy vs Momentum Scaling

Calculations for like metal impact of aluminum, iron, and lead are available from the instant of impact until the pressure has decreased to about 0.2 Mbar. Strain-rate and strength effects may begin to become important at these final

pressures, the hydrodynamic model has been a valid approximation to this point. The hydrodynamic equations may be put into a dimensionless form, but not the equation of state since it is an empirical fit. Except for this it would clearly be possible to apply the results, with the proper scaling factors, to any geometrically similar impact situation at the same velocity and the same material.

To determine if the equation-of-state form prevents direct scaling, the lead-lead impact at 2.0 cm/μsec was re-run with the configuration scaled up in dimension by a factor of 3. The results were practically identical to the scaled version. Since the form of the equation of state is identical for all the metals considered, it was concluded that scaling is justified in the hydrodynamic regime for similar geometries of a given metal and impact velocity.

The calculations at hand are sufficient to resolve the fundamental problem of whether the depth of penetration of a projectile is determined by the momentum of the impacting projectile, by the projectile's kinetic energy at impact, or by a combination of the two.

The momentum and energy hypotheses have been tested for all three metals by comparing the impact calculations at $v_0 = 2.0$ cm/μsec with the impact calculations at $v_0 = 0.76$ cm/μsec, where the latter are scaled to give either equal energy or equal momentum:

Equal energy

$$L = l = 0.26192 \text{ cm} \qquad v_0 = 2.0 \text{ cm}/\mu\text{sec}$$

$$L'/L = (v_0/v_0')^{2/3} = 1.906 \qquad v_0' = 0.76 \text{ cm}/\mu\text{sec}$$

$$\text{mass}'/\text{mass} = (L'/L)^3 = (v_0/v_0')^2 = 6.9252$$

Equal Momentum

$$L = l = 0.26192 \text{ cm} \qquad v_0 = 2.0 \text{ cm}/\mu\text{sec}$$

$$L'/L = (v_0/v_0')^{1/3} = 1.38 \qquad v_0' = 0.76 \text{ cm}/\mu\text{sec}$$

$$\text{mass}'/\text{mass} = (L'/L)^3 = v_0/v_0' = 2.632$$

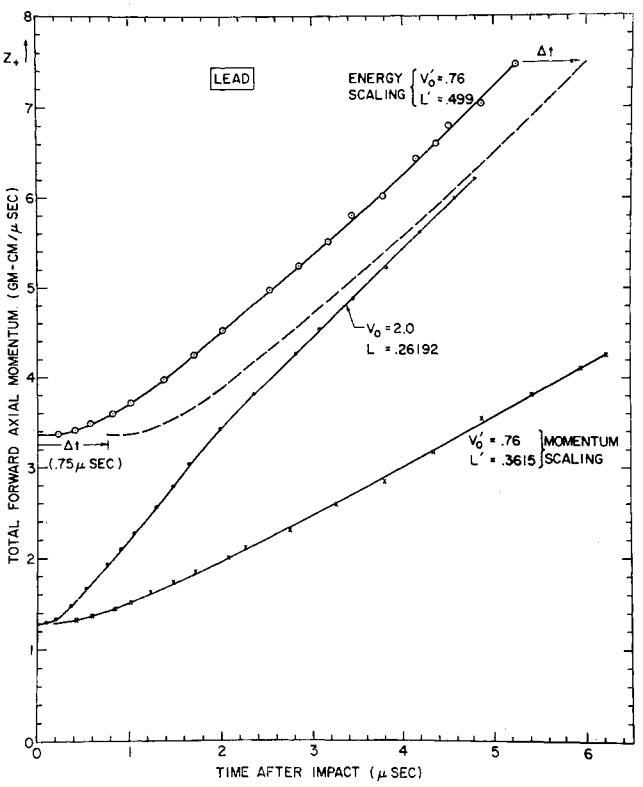

Fig. 6 Total forward momentum in a thick target as a function of the time since impact of a lead projectile and target.

For aluminum, calculations at $v_0 = 4.0$ and $v_0 = 6.0$ cm/μsec are also available, and these have also been scaled for comparison with the calculations at $v_0 = 2.0$ cm/μsec. The corresponding formulas for penetration depth are:

Equal Energy

$$P_e/L = K_e v_0^{2/3} \tag{5a}$$

Equal Momentum

$$P_e/L = K_m v_0^{1/3} \tag{5b}$$

Two important characteristics of the flow field are the total forward momentum and the total outward radial momentum present within the target at any instant of time:

$$Z_+ = \sum_{i,j} M_{i,j}(v_+)_{i,j} \qquad R_+ = \sum_{i,j} M_{i,j}(u_+)_{i,j} \tag{6}$$

The plus indicates that the sums are extended only over positive values of u and v. These quantities are computed during each cycle of the calculations. Their values may also be scaled. For example, the results at $v_0 = 0.76$ cm/μsec under the hypothesis of equal energy are scaled by multiplying R_+ and Z_+ by 6.9252 and length and time by 1.906. Momentum scaling requires that R_+ and Z_+ be multiplied by 2.632 and that length and time be multiplied by 1.38. Representative results are given in Figs. 6 and 7.

In Fig. 6 the calculated total forward axial momentum is plotted as a function of time for lead impact at $v_0 = 2.0$ cm/μsec. Also shown for comparison are the total forward axial momentum when the $v_0 = 0.76$ cm/μsec results are energy scaled and when they are momentum scaled. In Fig. 7 the calculated total outward radial momentum is shown for the same three impact situations.

It is clear from these results that momentum scaling cannot be justified, but energy scaling of the results of the $v_0' = 0.76$ calculations gives values of Z_+ and R_+ that become closer to the $v_0 = 2.0$ cm/μsec values as time is increased. If one only considers these total momentum curves, it appears that energy scaling slightly overestimates the velocity dependence of the hypervelocity damage mechanism and that the expon-

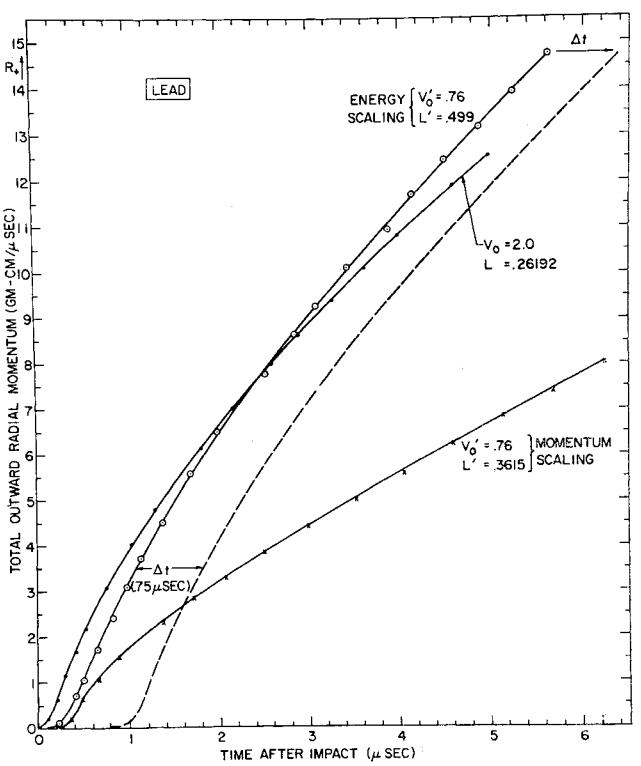

Fig. 7 Total positive radial momentum in a thick target at indicated time since lead-lead impact.

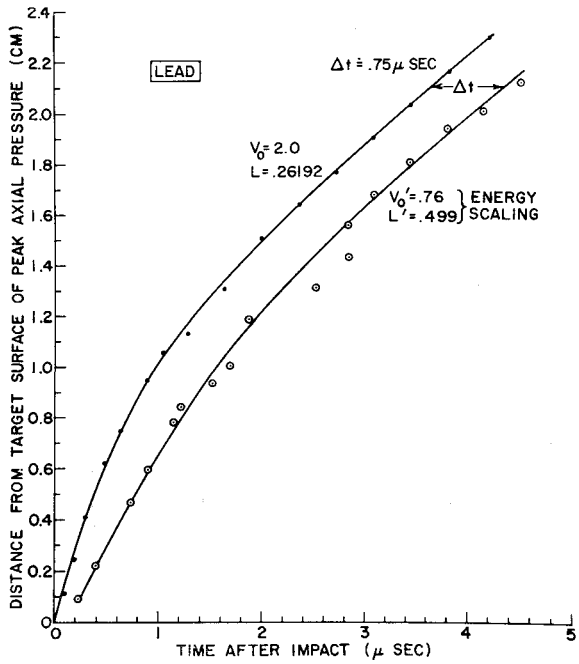

Fig. 8 The position of the peak axial pressure as a function of time for lead-lead impact.

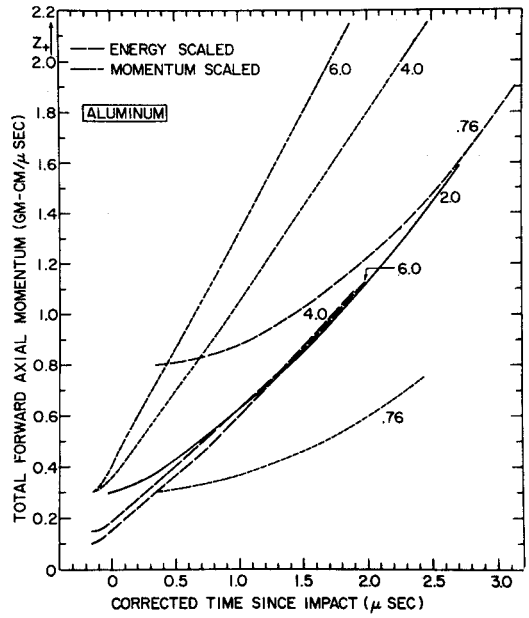

Fig. 10 Total forward momentum in the target as a function of the corrected time since impact of an aluminum projectile and a thick aluminum target; the numbers on the curves indicate the various impact velocities.

ent in the penetration formula (5) should be slightly smaller than $\frac{2}{3}$. This was the conclusion of Walsh and Tillotson.[5] They found that an exponent between 0.58 and 0.72 brought their energy equivalent Z_+ and R_+ curves into close agreement. Different values of the exponent were required for different velocity ranges and for different metals.

The results discussed in the next section show that this apparent variation in the exponent for different materials and velocity ranges may be explained by the failure to account for a time differential when comparing equivalent energy impacts.

Threshold of Energy Scaling

When comparing the deformation waves associated with two impact velocities of equivalent energy $v_0 > v_0'$, the characteristics during the initial stages are of course quite distinct.

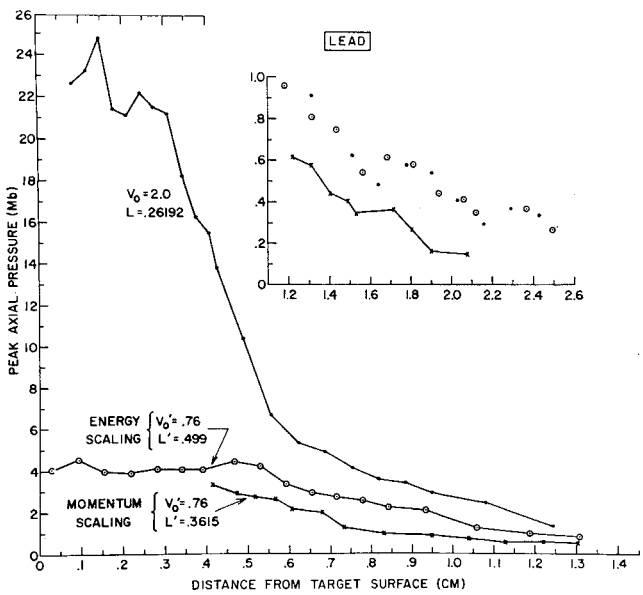

Fig. 9 Peak axial pressure in lead shown or function of distance below the original surface of a thick target.

The higher velocity projectile will produce larger pressures upon impact, and the pressure pulse will propagate at a faster velocity into the target. The pressure pulse associated with the lower velocity will require more time to reach a specific distance below the target surface.

To determine the time lag Δt between pressure pulses of equal energy, the peak axial pressure has been studied. In Fig. 8, for example, the distance of the peak axial pressure below the original target surface is plotted as a function of the time for lead-lead impact at $v_0 = 2.0$ cm/μsec and for the energy equivalent situation for impact at $v_0' = 0.76$ cm/μsec. A time lag of $\Delta t \doteq 0.75$ μsec is indicated.

Since the pressure pulse is the basic cause of the cratering process, two impact situations should be compared at times when the pulses are equal distance below the target surface. Accordingly, the energy scaled versions of Z_+ and R_+ in Figs. 6 and 7 should be shifted to the right a distance corresponding to $\Delta t = 0.75$ μsec.¶ In each figure the dashed curve represents the energy scaled version with the appropriate time correction. This correction leads to agreement between the energy equivalent impact situations, at least within the accuracy of the calculations.

In Fig. 9, the magnitude of the peak axial pressure pulse as a function of the distance below the surface of a lead target is shown for $v_0 = 2.0$ cm/μsec and for the momentum and energy equivalent versions of the $v_0' = 0.76$ cm/μsec calculations. Impact energy scaling is seen to result in overlapping values for the pressures when $p < 1.0$ Mbar.

Energy scaling has also been found to lead to excellent agreement between impacts at $v_0 = 2.0$ cm/μsec and $v_0' = 0.76$ cm/μsec for aluminum-aluminum and iron-iron impact. Overlapping values for the pressure are, for these cases, attained when $p < 0.2$ and $p < 0.4$ Mbar, respectively.

Finally, in Figs. 10 and 11, respectively, the values of Z_+ and R_+ are shown for aluminum-aluminum impact at several velocities. These are composite plots in which the energy and momentum scaled versions of the $v_0 = 0.76$ cm/μsec, the $v_0 = 4.0$ cm/μsec, and the $v_0 = 6.0$ cm/μsec calculations are all shown for comparison with the results of the $v_0 = 2.0$

¶ The same shifting is required for the momentum scaled version but would only increase the disparity between the momentum equivalent situations.

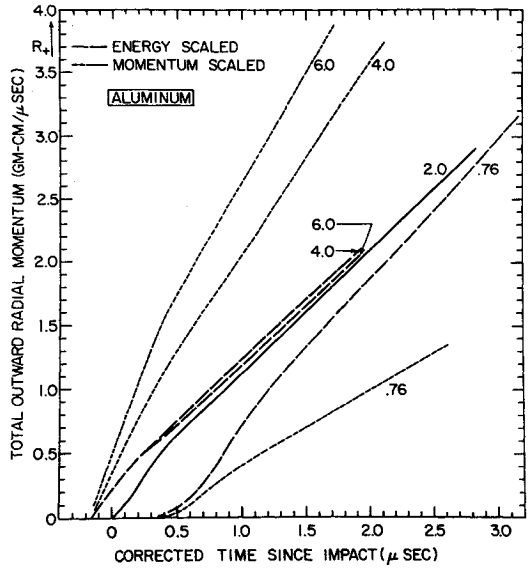

Fig. 11 Total positive radial momentum in a thick aluminum target as a function of the corrected time since impact by an aluminum projectile; the numbers on the curves indicate the various impact velocities.

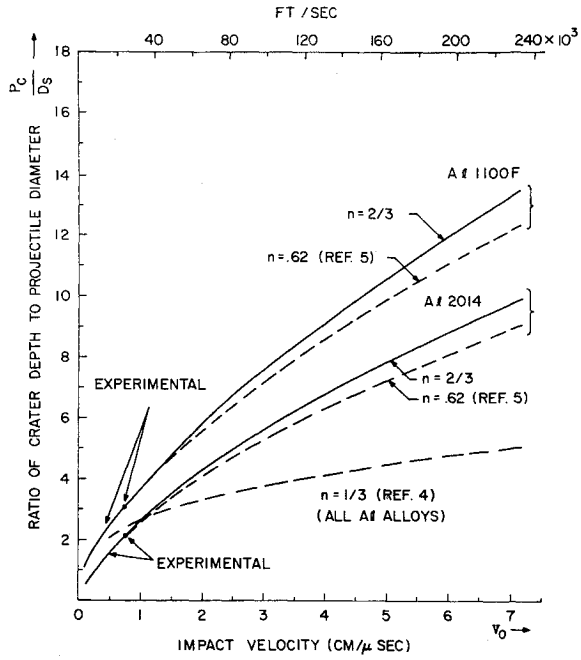

Fig. 12 Depth of penetration of aluminum projectiles impacting thick aluminum targets at a hypervelocity; the dashed curves are shown for comparison purposes.

cm/μsec values. The appropriate time corrections Δt have already been included in the plots. Excellent agreement is apparent for the energy equivalent impact situations.

Conclusions

Two impact situations are compared at times when the location of their peak pressures are an equal distance below the target surface. For equivalence of two impact cratering processes in a given material, it is required that at these corresponding times the total forward axial momentum Z_+, the total outward radial momentum R_+, and the amplitude of the pressure pulse become equal prior to the onset of strength and strain-rate effects. This criterion for equivalence is satisfied by the impact of geometrically similar projectiles of the same metal into a thick target of like metal provided the projectiles are of equal kinetic energy and the impact velocity exceeds a threshold value for energy scaling. This has been concluded from a detailed study of aluminum-aluminum, iron-iron, and lead-lead impact at $v_0 = 0.76$, 2.0, 4.0, and 6.0 cm/μsec. The calculations were carried out for cylindrical projectiles of radius equal to length, $L = l$.

The formula for the depth of penetration corresponding to the preceding qualifications is

$$P_c/L = K_e v_0^{2/3} \qquad (v_0 \geqq v_0^*) \tag{7}$$

where v_0^* is the threshold velocity for the $\frac{2}{3}$ law for a particular metal and K_e the corresponding experimental constant. These parameters are known from experiment to vary among alloys of nominally the same metal, reflecting strength and strain-rate effects that in the later stages of the process determine the final crater dimensions. If experimental data show that the penetration of geometrically similar projectiles into the target of a given alloy varies according to (7) at the upper end of the experimental range, it is safe to extrapolate at least to $v_0 = 6.0$ cm/μsec.

A corollary to this is that if the $\frac{2}{3}$ law is attained for two alloys of the same metal but with different values of K_e, this difference will persist. Strength and strain-rate effects will not disappear with increasing impact velocity. They will continue to become predominant during the latter stages of the cratering process.

To demonstrate the importance of the strength and strain-rate effects, the experimental data of Halperson[17] have been used for the energy scaling of aluminum-aluminum impact. Impact of aluminum spheres into both 1100F and 2014 aluminum are considered. In Fig. 12, Halperson's purely empirical formulas are plotted up to the velocity $v_0 = 0.76$ cm/μsec, which closely corresponds to the limit of his data. The solid-line curves at higher velocities show the extrapolations based on the energy scaling. Also shown for comparison are the corresponding extrapolations of Walsh and Tillotson ($\bar{n} = 0.62$) and the predictions of Bjork ($n = \frac{1}{3}$).

With the controversy between momentum and energy scaling apparently resolved, it is anticipated that experimentalists and theorists will direct increasing attention to the more practical geometries for the targets and more likely projectile materials in the case of meteoroid simulation. Some early results of studies of the penetration of thin plate targets have recently become available.[10]

Appendix

Let ρ, p, $\mathbf{u} = (u, 0, v)$, and I denote the density, pressure, velocity, and specific internal energy, respectively. Then the axisymmetric formulation of the visco-plastic equations may be written in the form:

Mass

$$\frac{\partial \rho}{\partial t} + u\frac{\partial \rho}{\partial r} + v\frac{\partial \rho}{\partial z} + \rho \operatorname{div} \mathbf{u} = 0 \tag{A1}$$

Radial Momentum

$$\rho\left(\frac{\partial u}{\partial t} + u\frac{\partial u}{\partial r} + v\frac{\partial u}{\partial z}\right) = \frac{\partial}{\partial r}\left(P + S_{rr}\right) + \frac{S_{rr} - S_{\theta\theta}}{r} + \frac{\partial S_{rz}}{\partial z} \tag{A2}$$

Axial Momentum

$$\rho\left(\frac{\partial v}{\partial t} + u\frac{\partial v}{\partial r} + v\frac{\partial v}{\partial z}\right) = \frac{\partial}{\partial z}\left(P + S_{zz}\right) + \frac{1}{r}\frac{\partial}{\partial r}\left(rS_{rz}\right) \tag{A3}$$

Energy

$$\rho\left(\frac{\partial I}{\partial t} + u\frac{\partial I}{\partial r} + v\frac{\partial I}{\partial z}\right) + p\,\mathrm{div}\mathbf{u} = \mu D^2 \qquad \text{(A4)}$$

Here the flow is assumed to be strictly adiabatic and the following notations have been introduced:

$$\left.\begin{aligned}
P &= -p - \tfrac{2}{3}\mu\,\mathrm{div}\mathbf{u} \qquad \mathrm{div}\mathbf{u} = \frac{1}{r}\frac{\partial(ru)}{\partial r} + \frac{\partial v}{\partial z}\\
S_{zz} &= \mu D_{zz} = 2\mu(\partial v/\partial z)\\
S_{rr} &= \mu D_{rr} = 2\mu(\partial u/\partial r)\\
S_{rz} &= \mu D_{rz} = \mu\left(\frac{\partial u}{\partial z} + \frac{\partial v}{\partial r}\right)\\
S_{\theta\theta} &= \mu D_{\theta\theta} = 2\mu(u/r)\\
D^2 &= D_{rz}^2 + \tfrac{1}{2}(D_{rr}^2 + D_{\theta\theta}^2 + D_{zz}^2) - \tfrac{2}{3}(\mathrm{div}\mathbf{u})^2\\
\tau^2 &= \mu^2 D^2 \qquad \tau_{ij} = P\delta_{ij} + S_{ij}
\end{aligned}\right\} \qquad \text{(A5)}$$

References

[1] Bruce, E. P., "Review and analysis of high speed impact data," *Proceedings of the Fifth Symposium on Hypervelocity Impact* (Armed Services Technical Information Agency, 1962), Vol. I, Part 2, pp. 439–474.

[2] Herrman, W. and Jones, A. H., "Correlation of hypervelocity impact data," *Proceedings of the Fifth Symposium on Hypervelocity Impact* (Armed Services Technical Information Agency, 1962), Vol. I, Part 2, pp. 389–438.

[3] Anonymous, "Study of target penetration prediction by high speed and ultra-high speed ballistic impact," Eglin Air Force Base APGC-TDR-63-23 (April 1963).

[4] Bjork, R. L., "Effects of a meteoroid impact on steel and aluminum in space," Rand Corp. Rept. P-1662 (December 1958).

[5] Walsh, J. M. and Tillotson, J. H., "Hydrodynamics of hypervelocity impact," *Proceedings of the Sixth Symposium on Hypervelocity Impact* (Armed Services Technical Information Agency, 1963), Vol. II, Part 1, pp. 59–104.

[6] Eichelberger, R. J., "Theoretical and experimental studies of crater formation," *Proceedings of the Sixth Symposium on Hypervelocity Impact* (Armed Services Technical Information Agency), Vol. II, Part 2, pp. 683–706.

[7] Heldenfels, R. R. and Hurlich, A., "Structures and materials-state of the art," Astronautics Aerospace Eng. **1**, 75–80 (November 1963).

[8] Riney, T. D., "Theory of high speed impact," Eglin Air Force Base, APGC-TDR-62-20 (March 1962).

[9] Riney, T. D., "Behavior of metals during hypervelocity impact cratering," *Developments in Mechanics* (Pergamon Press, Oxford, England, 1964), pp. 419–445.

[10] Riney, T. D., "Theoretical hypervelocity impact calculations using the PICWICK code," General Electric TIS Rept. R64SD13 (February 1964).

[11] Symond, P. S. and Ting, T. C. T., "Longitudinal impact on viscoplastic rods—approximate methods and comparisons," Brown Univ. Div. Engineering TR to Advanced Research Projects Agency, Contract SD-86 (August 1963).

[12] Harlow, F. H., "Two-dimensional hydrodynamics calculations," Los Alamos Science Lab. Rept. LA-2301 (September 1959).

[13] Riney, T. D., "Solution of visco-plastic equations for axisymmetric hypervelocity impact," Eglin Air Force Base APGC-TDR-62-74 (December 1962).

[14] Riney, T. D., "Visco-plastic solution of hypervelocity impact cratering phenomenon" *Proceedings of the Sixth Symposium on Hypervelocity Impact* (Armed Services Technical Information Agency, 1963), Vol. II, Part 1, pp. 105–140.

[15] Jones, O. E., Neilson, F. W., and Benedick, W. B., "Dynamic yield behavior of explosively loaded metals determined by a quartz transducer technique," J. Appl. Phys. **33**, 3224–3232 (1962).

[16] Heyda, J. F. and Riney, T. D., "Penetration of structures by hypervelocity projectiles," General Electric TIS Rept. R64SD3 (February 1964).

[17] Halperson, S. M., "Some phenomena associated with impacts into aluminum," *Proceedings of the Sixth Symposium on Hypervelocity Impact* (Armed Services Technical Information Agency, 1963), Vol. II, Part 2, pp. 525–542.